Luminescence optical tomography of dense scattering media

Jenghwa Chang

Department of Pathology, State University of New York Health Science Center at Brooklyn, Brooklyn, New York 11203

Harry L. Graber

Department of Physiology and Biophysics, State University of New York Health Science Center at Brooklyn, Brooklyn, New York 11203

Randall L. Barbour

Department of Pathology and Department of Physiology and Biophysics, State University of New York Health Science Center at Brooklyn, Brooklyn, New York 11203

Received April 3, 1996; revised manuscript received June 7, 1996; accepted June 14, 1996

Using a set of coupled radiation transport equations, we derive image operators for luminescence optical tomography with which it is possible to reconstruct concentration and mean lifetime distribution from information obtained from dc and time-harmonic optical sources. Weight functions and detector readings were computed from analytic solutions of the diffusion equation and from numerical solutions of the transport equation by Monte Carlo methods. Detector readings were also obtained from experiments on vessels containing a balloon filled with dye embedded in an Intralipid suspension with dye in the background. Image reconstructions were performed by the conjugate gradient descent method and the simultaneous algebraic reconstruction technique with a positivity constraint. A concentration correction was developed in which the reconstructed concentration information is used in the mean-lifetime reconstruction. The results show that the target can be accurately located in both the simulated and the experimental cases, but quantitative inaccuracies are present. Observed errors include a shadowing effect in regions that have the lowest weight within the inclusion. Application of the concentration correction can significantly improve computational efficiency and reduce error in the mean-lifetime reconstructions. © 1997 Optical Society of America. [S0740-3232(97)01901-7]

1. INTRODUCTION

The use of perturbation methods in optical imaging of tissues has attracted significant and increasing interest in recent years.[1–3] This approach involves applying the difference between measurements obtained at the boundary of reference and test media to reconstruct a cross-sectional image. The difference signal is usually small relative to the two quantities that are being compared and is sensitive to noise. This situation represents an intrinsically more difficult measurement than, for example, the case of fluorescence measurements, for which the increase in signal that is due to the added fluorophore is usually much larger than the background signal. Fluorescence measurements also offer the distinct advantage that fluorophores that are reactive to their immediate chemical environments can be synthesized. A broad range of probes has been developed for use in studying a range of biochemical and cellular processes, the emission properties of which are dependent on, among other things, local pH, metal ion concentration, or potential difference.

Recently several groups of researchers have reported the use of luminescence techniques in a tomographic imaging mode.[4–7] This application is potentially appealing and has similarities to more-traditional radioscintigraphic imaging methods such as single-photon emission computed tomography and positron emission tomography. There are, however, many potential advantages to luminescence tomography. As mentioned above, in contrast to radioactivity, luminescence can be environment sensitive. Luminescence measurements can be vastly more sensitive than measurements involving radioisotopes, and the radiation emitted is not damaging to tissue. The former is especially true at near-infrared wavelengths, at which autofluorescence levels are very low.

In this paper we extend recent studies[4,5] and describe the use of perturbation methods to produce lifetime and concentration images of lumiphores added to a homogeneous dense scattering medium. A transport-theory-based imaging operator is also derived that contains a correction for lumiphore saturation and represents a more general formulation than previously reported.[6,7] The final form of this operator is a system of linear equations that can easily be solved by iterative methods. We have studied excitation and emission in the luminescence phenomenon, using two coupled one-speed transport equations. Two modulation frequencies, dc and 100 MHz, were applied to yield required information for the reconstruction of the product of concentration, microscopic cross section, and quantum yield, and of mean life-

0740-3232/97/010288-12$10.00

time, respectively. We performed numerical simulations to calculate the diffusion-regime limiting form of this operator for a specific test medium. Experimental data were collected with a computed tomography–type laser scanning system. Images were reconstructed by the conjugate gradient descent (CGD) method[8] and the simultaneous algebraic reconstruction technique (SART).[9,10] A concentration correction technique was also developed to make use of the concentration information reconstructed from the dc data to improve computational efficiency and reduce errors in the mean-lifetime reconstructions.

2. THEORY

The excitation light and the emission light associated with a luminescence process are governed by a set of coupled time-dependent radiative transfer equations[11,12]:

$$\frac{1}{c}\frac{\mathrm{d}\phi_1}{\mathrm{d}t} + \mathbf{\Omega}\cdot\nabla\phi_1 + (\mu_{T,1} + \mu_{T,1\to 2})\phi_1 = q_1 + \int_{4\pi}\mu_{s,1}(\mathbf{\Omega}'\cdot\mathbf{\Omega})\phi_1'\mathrm{d}\Omega', \quad (1)$$

$$\frac{1}{c}\frac{\mathrm{d}\phi_2}{\mathrm{d}t} + \mathbf{\Omega}\cdot\nabla\phi_2 + \mu_{T,2}\phi_2 = q_2 + \int_{4\pi}\mu_{s,2}(\mathbf{\Omega}'\cdot\mathbf{\Omega})\phi_2'\mathrm{d}\Omega', \quad (2)$$

where the subscripts 1 and 2 denote, respectively, the excitation and the emitted light; c is the speed of light; $\mathrm{d}\Omega$ is the differential solid angle (sr); ϕ_1 and ϕ_2 are the angular intensities ($\mathrm{cm}^{-2}\ \mathrm{s}^{-1}\ \mathrm{sr}^{-1}$); q_1 and q_2 are the angular source strengths ($\mathrm{cm}^{-3}\ \mathrm{s}^{-1}\ \mathrm{sr}^{-1}$); $\mu_s(\mathbf{\Omega}'\cdot\mathbf{\Omega})$ is the macroscopic differential scattering cross section ($\mathrm{cm}^{-1}\ \mathrm{sr}^{-1}$); μ_T is the macroscopic total cross section (cm^{-1}); and $\mu_{T,1\to 2} = N_g\,\Sigma_{T,1\to 2}$ is the change in total cross section after the lumiphore is added, where $\Sigma_{T,1\to 2}$ is the microscopic total cross section (cm^2) of the lumiphore and N_g is the concentration of lumiphore in the electronic ground state. In addition, it is convenient to define the following quantities for later use: $\mu_{s,i} = \int_{4\pi}\mu_{s,i}(\mathbf{\Omega}'\cdot\mathbf{\Omega})\mathrm{d}\Omega'$ is the macroscopic scattering cross section (cm^{-1}), $\mu_{a,i} = \mu_{T,i} - \mu_{s,i}$ is the macroscopic absorption cross section (cm^{-1}), and $\mu_{s,i}' = (1 - f_{1,i})\mu_{s,i}$ is the reduced scattering cross section (cm^{-1}), where $f_{1,i} = \int_{4\pi}\mu_{s,i}(\mathbf{\Omega}'\cdot\mathbf{\Omega})\mathbf{\Omega}'\cdot\mathbf{\Omega}\mathrm{d}\mathbf{\Omega}/\int_{4\pi}\mu_{s,i}(\mathbf{\Omega}'\cdot\mathbf{\Omega})\mathrm{d}\Omega$ is the first moment of the differential scattering cross section; $i = 1, 2$ in all cases.

In this paper we assume either that there is no significant overlap of the absorption and emission spectra or that the total lumiphore concentration N_0 is low throughout the medium under investigation. In either case there are two important consequences. First, we can consider only a single frequency in the emission spectrum without loss of generality, as the transport equations for light emitted [Eq. (2)] at different wavelengths will be coupled with the transport equation for the excitation light [Eq. (1)], but not with one another. Second, the absorption rate for excitation light by the lumiphore is much greater than that for emission light, and the rate for spontaneous emission greatly exceeds that for induced emission. Then the coupling between the two transport equations is governed by

$$\frac{\mathrm{d}N_g}{\mathrm{d}t} = -\Sigma_{T,1\to 2}\,\bar{\phi}_1 N_g + \frac{1}{\tau}N_e, \quad (3)$$

where $N_e = N_0 - N_g$ is the concentration of excited lumiphore, N_0 is the total lumiphore concentration (ground and excited states), $\bar{\phi}_1 = \int_{4\pi}\phi_1\mathrm{d}\Omega$ is the intensity ($\mathrm{cm}^{-2}\ \mathrm{s}^{-1}$) of the excitation light, and τ is the mean lifetime of the fluorescent probe's excited states (see Appendix A). Thus the emission source term q_2 in Eq. (2) is

$$q_2 = \frac{\gamma}{4\pi\tau}N_e, \quad (4)$$

where γ is the (dimensionless) quantum yield of the lumiphore.

Let R be the reading of a given detector for the emitted intensity and r_2 be the corresponding detector sensitivity function, i.e., $r_2 = r_2(\mathbf{r}, \Omega, t)$. Then R is the time convolution of r_2 and the intensity of the luminescent emission. The latter is in turn a time convolution of the emission source and the Green's function. By appropriately reordering the integrations and applying a well-known reciprocity theorem,[12] we obtain

$$R = \int_v\int_{4\pi} r_2 \otimes \left[\int_{v'}\int_{4\pi} q_2' \otimes G_2(\mathbf{r}, \mathbf{\Omega}; \mathbf{r}', \mathbf{\Omega}'; t)\mathrm{d}\Omega'\mathrm{d}^3r'\right]\mathrm{d}\Omega\mathrm{d}^3r = \frac{1}{4\pi}\int_v \frac{\gamma}{\tau}N_e \otimes \bar{\phi}_2^{+}\,\mathrm{d}^3r, \quad (5)$$

where $\otimes$ denotes a convolution in time, N_e is the concentration of lumiphore in the excited state at $\mathbf{r}$, $G_2(\mathbf{r}, \mathbf{\Omega}; \mathbf{r}', \mathbf{\Omega}'; t)$ is the Green's function at $\mathbf{r}$ in direction $\mathbf{\Omega}$ with the source located at $\mathbf{r}'$ in direction $\mathbf{\Omega}'$, and $\bar{\phi}_2^{+} = \int_{4\pi}\int_{v'}\int_{4\pi} r_2'\otimes G_2(\mathbf{r}, -\mathbf{\Omega}; \mathbf{r}', -\mathbf{\Omega}'; t)\mathrm{d}\Omega'\mathrm{d}^3r'\,\mathrm{d}\Omega$ is the adjoint intensity, which can be interpreted as the intensity at $\mathbf{r}$ that arises from a source whose distribution in space, direction, and time is r^2.

In the frequency domain one obtains detector readings by Fourier transforming Eq. (5):

$$\tilde{R} = \frac{1}{4\pi}\int_v \frac{\gamma}{\tau}\tilde{N}\tilde{\bar{\phi}}_2^{+}\,\mathrm{d}^3r, \quad (6)$$

where $\tilde{}$ denotes the Fourier transform. Let N_0 be the total lumiphore concentration; the Fourier transform of Eq. (3) then becomes

$$(1 + j\omega\tau)\tilde{N}_g + \frac{\tau\Sigma_{T,1\to 2}}{2\pi}\tilde{\bar{\phi}}_1 \otimes \tilde{N}_g = 2\pi N_0\delta(\omega), \quad (7a)$$

$$\tilde{N}_e = 2\pi N_0\delta(\omega) - \tilde{N}_g, \quad (7b)$$

where $j = \sqrt{-1}$, and $\otimes$ now denotes a convolution in frequency.

Under a time-varying excitation the lumiphore ground-state concentration is not constant because of the continu-

ous shifts in the rates of population and depopulation of that state. Consequently a time-harmonic excitation will produce an anharmonic periodic signal containing the fundamental frequency and all its overtones; this occurs when the population of the excited state becomes appreciable, i.e., when the lumiphore is partially saturated. This situation is problematic because subsequent analysis to infer properties of an unknown medium would require consideration of all these frequencies. The excitation intensity at which saturation effects would need to be considered is greater than the intensities currently used for most biological studies[5] (i.e., up to $\sim 10^{20}$ photons cm^{-2} s^{-1}). However, for long-lived fluorophores ($\tau \sim 1$ μs) or even longer-lived phosphors ($\tau \sim 1$ ms) saturation may become significant.

Let $\tilde{\bar{\phi}}_1$ be a time-harmonic excitation. That is, let $\tilde{\bar{\phi}}_1$ be equal to $2\pi\bar{\phi}_1{}^0[\delta(\omega) + \eta'\delta(\omega - \omega_0) + \eta''\delta(\omega + \omega_0)]$, with $\eta' = \eta \exp(-j\varphi)/2$ and $\eta'' = \eta \exp(j\varphi)/2 = \eta'$, where η is the modulation and φ is the phase. Then Eqs. (7) can be solved by means of the following approximations. When the saturation level is insignificant, i.e., $N_g \approx N_0$, we have

$$\tilde{N}_g(0) = 2\pi N_0(1 - \tau\Sigma_{T,1\to 2}\bar{\phi}_1{}^0)\delta(0), \tag{8a}$$

$$\tilde{N}_g(\omega_0) = -\tilde{N}_e(\omega_0) = -\frac{2\pi\tau\Sigma_{T,1\to 2}N_0\bar{\phi}_1{}^0\eta'}{1 + j\omega_0\tau}\delta(0). \tag{8b}$$

These equations, which are essentially zeroth-order approximations to the solutions of Eqs. (7), are applicable when $\tau\Sigma_{T,1\to 2}\bar{\phi}_1{}^0 \ll 1$.[5] For a typical fluorophore with $\tau = 10^{-9}$ s and $\Sigma_{T,1\to 2} = 5 \times 10^{-17}$ cm^2, this criterion corresponds to an allowable excitation of $\bar{\phi}_1{}^0 = 2 \times 10^{23}$ photons per unit area (cm^2) and unit time (s); a more detailed discussion of this calculation is available elsewhere.[5] When the saturation level is more significant, coupling between dc and the fundamental frequency and its first overtone should be considered, but the contribution of higher-order harmonics can be ignored, permitting the following first-order approximations to the solutions of Eqs. (7):

$$\tilde{N}_g(0) = \frac{2\pi N_0}{1 + \tau\Sigma_{T,1\to 2}\bar{\phi}_1{}^0}\delta(0) \times \frac{2(1 + \tau\Sigma_{T,1\to 2}\bar{\phi}_1{}^0)^2 + 2(\omega_0\tau)^2}{2(1 + \tau\Sigma_{T,1\to 2}\bar{\phi}_1{}^0)^2 + 2(\omega_0\tau)^2 - (\tau\Sigma_{T,1\to 2}\eta\bar{\phi}_1{}^0)^2}, \tag{9a}$$

$$\tilde{N}_g(\omega_0) = -\tilde{N}_s(\omega_0) = \frac{2\pi N_0}{1 + \tau\Sigma_{T,1\to 2}\bar{\phi}_1{}^0}\delta(0) \times \frac{-2\tau\Sigma_{T,1\to 2}\bar{\phi}_1{}^0\eta'(1 + \tau\Sigma_{T,1\to 2}\bar{\phi}_1{}^0 - j\omega_0\tau)}{2(1 + \tau\Sigma_{T,1\to 2}\bar{\phi}_1{}^0)^2 + 2(\omega_0\tau)^2 - (\tau\Sigma_{T,1\to 2}\eta\bar{\phi}_1{}^0)^2}. \tag{9b}$$

See Appendix B for detailed derivations of Eqs. (9a) and (9b) and the procedure for generating higher-order approximations.

The goal of the inverse problem is to solve Eq. (6) for $\mu_{T,1\to 2}$, γ, and τ under different source and detection conditions. Doing this requires two reconstruction steps. In the first step we solve for the background absorption and scattering coefficients, μ_a and μ_s, respectively, of the medium for the excitation and the emission photons separately, using previously developed techniques.[13] The second step is to reconstruct $\mu_{T,1\to 2}$, γ, and τ with estimates of $\tilde{\bar{\phi}}_1$ and $\tilde{\bar{\phi}}_2{}^+$ that are calculated with the coefficients obtained from the first step. The following are two proposed methods for this second step.

A. dc Source

If we use dc sources, that is, if $\eta' = 0$, then we have $\tilde{\bar{\phi}}_1 = 2\pi\bar{\phi}_1{}^0\delta(0)$, $\tilde{\bar{\phi}}_2 = 2\pi\bar{\phi}_2{}^0\delta(0)$, and

$$\tilde{N}_e = \frac{\tau\Sigma_{T,1\to 2}N_0}{1 + \tau\Sigma_{T,1\to 2}\bar{\phi}_1{}^0}\tilde{\bar{\phi}}_1 = \tau\Sigma_{T,1\to 2}N_g\tilde{\bar{\phi}}_1.$$

Equation (6) becomes

$$\tilde{R} = \frac{1}{4\pi}\int_v \tilde{\bar{\phi}}_1\tilde{\bar{\phi}}_2{}^+(\gamma\Sigma_{T,1\to 2}N_g)\mathrm{d}^3r = \int_v w(\gamma\Sigma_{T,1\to 2}N_g)\mathrm{d}^3r = \int_v w\frac{\gamma\tau\Sigma_{T,1\to 2}N_0}{1 + \tau\Sigma_{T,1\to 2}\bar{\phi}_1{}^0}\mathrm{d}^3r, \tag{10}$$

where $w \equiv w_{\mathrm{dc}} = \tilde{\bar{\phi}}_1\tilde{\bar{\phi}}_2{}^+/4\pi$ is the weight function. If $\tilde{\bar{\phi}}_1$and $\tilde{\bar{\phi}}_2{}^+$ can be precalculated under the assumption that lumiphore is not present, then we can compute the unknown quantity $\gamma\Sigma_{T,1\to 2}N_g$ or $\gamma\Sigma_{T,1\to 2}N_0/(1 + \tau\Sigma_{T,1\to 2}\bar{\phi}_1{}^0)$ by solving a linear system obtained by discretizing Eq. (10). If the saturation level is insignificant, then $\gamma\Sigma_{T,1\to 2}N_g \approx \gamma\Sigma_{T,1\to 2}N_0$, and if $\Sigma_{T,1\to 2}$ is known, then γN_0 can be obtained. Here, only the product of quantum efficiency and lumiphore concentration is found, and they cannot be directly separated.

B. ac Source

If modulated sources are used, and we adopt the approximation in Eq. (8b) and solve for $\gamma\Sigma_{T,1\to 2}N_0$ by analyzing the dc component of the response as described above, then Eq. (6) becomes

$$\tilde{R} = \int_v w\frac{1 - j\omega_0\tau}{1 + \omega_0{}^2\tau^2}\mathrm{d}^3r, \tag{11}$$

where $w \equiv w_{\mathrm{ac}} = \gamma\Sigma_{T,1\to 2}N_0\tilde{\bar{\phi}}\tilde{\bar{\phi}}_2{}^+/4\pi$. Equation (11) can be discretized, and the real and the imaginary parts of the detector readings give rise to a system of linear equations from which the real part, $1/(1 + \omega_0{}^2\tau^2)$, the imaginary part, $-\omega_0\tau/(1 + \omega_0{}^2\tau^2)$, and their ratio, $-\omega_0\tau$, of the unknowns can be reconstructed. Because ω_0 is known, τ can also be deduced. If the approximation in Eq. (9b) is adopted and $\gamma\Sigma_{T,1\to 2}N_0/(1 + \tau\Sigma_{T,1\to 2}\bar{\phi}_1{}^0)$ is solved from the dc signal, we get

$$\tilde{R} = \int_v \frac{w[2\eta'(1 + \tau\Sigma_{T,1\to 2}\bar{\phi}_1{}^0 - j\omega_0\tau)]\mathrm{d}^3r}{2(1 + \tau\Sigma_{T,1\to 2}\bar{\phi}_1{}^0)^2 + 2(\omega_0\tau)^2 - (\tau\Sigma_{T,1\to 2}\bar{\phi}_1{}^0\eta)^2}, \tag{12}$$

where w is the same as in Eq. (11). When $\tau\Sigma_{T,1\to2}{\phi_1}^0 \ll 1$, Eq. (12) reduces to Eq. (11). Otherwise, the ratio of the imaginary to the real parts of the unknown, $-\omega_0\tau/(1 + \tau\Sigma_{T,1\to2}{\phi_1}^0)$, can be reconstructed, and τ can be subsequently deduced.

3. SIMULATIONS AND EXPERIMENTS

A. Simulations

Analytic solutions of a three-dimensional diffusion equation for an infinite homogeneous medium, $\phi(\mathbf{r}_s, \mathbf{r}) = S_0 \exp(-j\kappa|\mathbf{r} - \mathbf{r}_s|)/(4\pi D|\mathbf{r} - \mathbf{r}_s|)$, where $D = 1/[3(\mu_a + \mu_s')]$ is the diffusion coefficient (in centimeters), $\kappa^2 = -\mu_a/D - j\omega/cD$ is the square of the complex wave number, S_0 is the source strength, and $\mathbf{r}_s$ is the source location, were calculated to yield the detector readings and weight functions for reconstruction. For detector-reading computations the excitation field in each volume element (voxel) was calculated by means of the above formula for $\phi(\mathbf{r}_s, \mathbf{r})$ and multiplied by the cross-section perturbation to yield the equivalent emission source. We then used the same formula, with $\mathbf{r}$ substituted for $\mathbf{r}_s$, $\mathbf{r}_d$ for $\mathbf{r}$ (where $\mathbf{r}_d$ is the detector location), and the equivalent emission source for S_0, to calculate the detector readings. The detector readings were corrupted with multiplicative Gaussian white noise at a level of 1% [i.e., (noise variance)/(signal amplitude) = 0.01]. Similarly, for the weight-function computations we used the formula for $\phi(\mathbf{r}_s, \mathbf{r})$ to compute the forward intensity, and the formula for $\phi(\mathbf{r}_d, \mathbf{r})$ with $S_0 = 1$ to compute the adjoint intensity, in every voxel. Figure 1 is an illustration of the phantom structure wherein an 8.0 cm × 8.0 cm × 0.2 cm square region of interest (ROI) was selected in an otherwise infinite medium. The target and the surrounding medium both have the same scattering and absorption cross sections for the excitation and emission fields; that is, $\mu_{s,1}' = \mu_{s,2}' = 1$ mm^{-1} and $\mu_{a,1} = \mu_{a,2} = 0.003$ mm^{-1}. The diffusion constant and the diffusion length (L, which is equal to $\sqrt{D/\mu_a}$; $-L^{-2}$ is the real part of κ^2) for this medium are, respectively, 0.33 and 5.74 mm. Lumiphore was uniformly distributed in a 1.2 cm × 1.2 cm × 0.2 cm region of the ROI [Fig. 1(B)], with $\mu_{T,1\to2} = 0.00001$ mm^{-1}, $\tau = 10^{-9}$ s, and $\gamma = 1$. Two sets of simulations were performed, with the lumiphore located in the center of the ROI in one case and in the lower half of the ROI in the other. Sources were located every 15° on a circle of 6.0-cm diameter about the center of the ROI. For each source, 39 detectors positioned every 9° on the same circle were used to collect emitted photons. Two modulation frequencies, dc and 100 MHz, were simulated to generate the required information for both $\gamma\mu_{T,1\to2}$ and mean-lifetime reconstructions, as described in Eqs. (10)–(12).

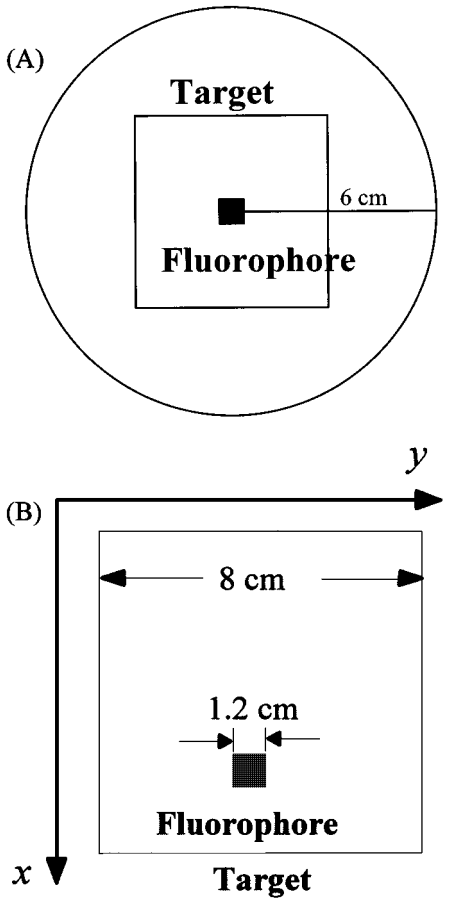

Fig. 1. Sketches of (A) the source–detector ring and (B) the phantom structure used for the diffusion computations.

B. Experiment

Figures 2(A) and 2(B) are, respectively, illustrations of the experimental tissue phantoms and the source and detector configurations. The experiment was performed with one balloon and added dye in the background. The 8-cm inner-diameter cylindrical vessel was filled with 0.33% Intralipid containing 0.1 μM Rhodamine 6G dye [$\tau \approx 4$ ns (Ref. 14) and $\Sigma_{T,1\to2} \approx 3.71 \times 10^{-16}$ cm^2]. The balloon's volume was 0.5 mL, and it contained dye at a concentration of 10 μM. A 0.75-W multiline (average wavelength ~500 nm) beam from a Coherent Innova 200–10 argon-ion laser source was used to irradiate the phantom. This corresponds to a photon energy of $(6.63 \times 10^{-34}$ J s$)$ $(3 \times 10^8$ m s$^{-1})/(5 \times 10^{-7}$ m$) \approx 4 \times 10^{-19}$ J, for a photon emission rate of $\sim 2 \times 10^{18}$ s^{-1}. For this combination of excitation level, mean lifetime, and total cross section there is no appreciable saturation of the fluorophore.[5] The 0.75-W excitation level was used only for the purpose of ensuring output stability of the laser and not because of any dearth of signal; in fact, for some measurements it was necessary to attenuate the measured fluorescence to avoid saturation of the detector. A Newport FS-1 RG.610 filter blocked excitation light from entering the detector. The detector was a Hamamatsu C3140 CCD camera directed normally to the phantom to collect the emission light. A limited illumination angle was used. The detectors were located every 30° about the cylinder, and the source was positioned every 30° from 90° to 270° counterclockwise relative to the source. Eighty-four detector readings were taken. The source intensity was recorded for each measurement by a Coherent Labmaster-E laser measurement system with a Model LM-3 detector head. Each measurement was then corrected for dark current, source intensity, and lens aperture. At least two measurements

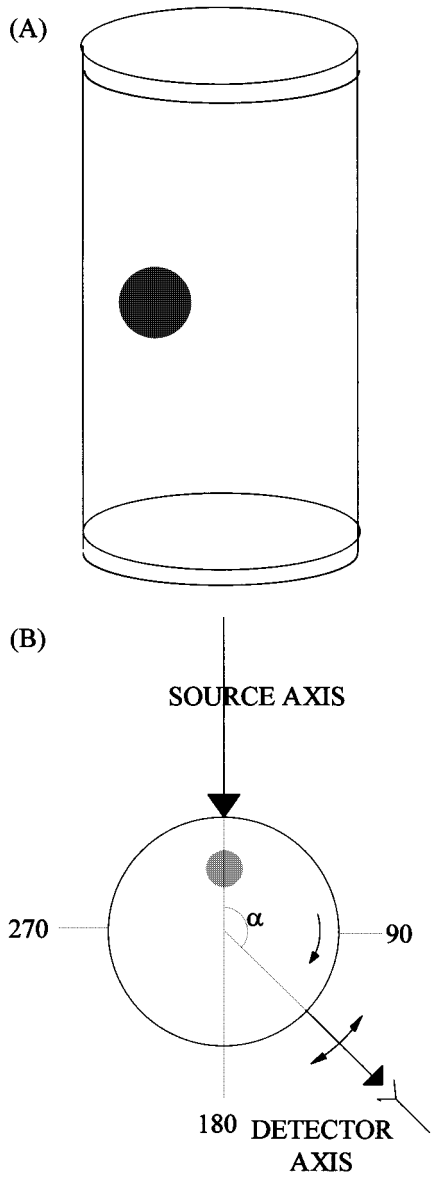

Fig. 2. (A) Tissue phantom for the experiment; one balloon was suspended in the cylinder. (B) Source and detector configurations.

were taken and averaged to yield the detector readings for each source–detector pair.

The optical thickness of the phantom medium was ~40 transport mean-free-path lengths (mfp) in diameter for both the excitation and the emission light.[15] Weight functions for the corresponding reference media were computed by Monte Carlo simulations, which assumed an optical thickness of 20 transport mfp. We are aware that use of these weight functions for studies involving the concentration of Intralipid used in these experiments introduces a systematic error. Nevertheless, we adopted them both as a means of testing the robustness of the imaging scheme and because in previous studies involving elastic scatter imaging we showed that systematic errors of this type for simply structured media do not appreciably influence the qualitative accuracy of the reconstruction.[16]

C. Image Reconstruction

Image reconstructions were performed with the CGD and SART algorithms, with positivity constraints on the reconstruction results and a matrix rescaling technique.[17] Each column of the weight matrix is normalized so that its largest element is equal to one; we observed that this can have the effect of accelerating convergence.[17] We performed two-dimensional reconstructions in the $x-y$ plane of the target [Fig. 1(B)], using the simulation data. The targets were sampled every 2 mm in both the x and the y directions, for a total of 41×41 or 1,681 voxels. For the experimental data we performed the reconstructions [Fig. 3(A)] by assuming that the target's properties

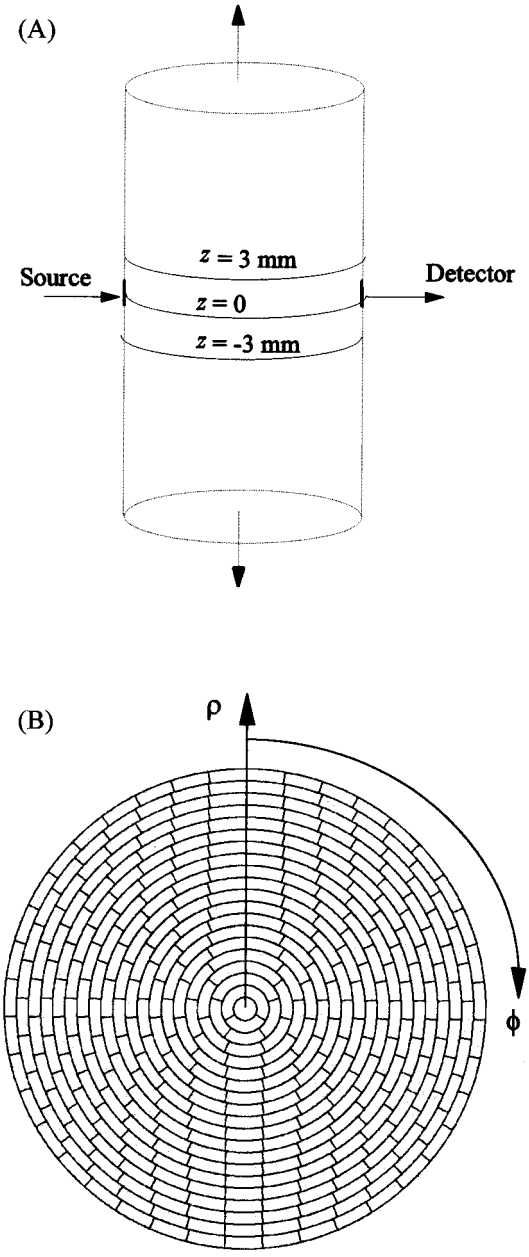

Fig. 3. (A) Schematic of two-dimensional reconstruction with translational invariance assumed along the z axis. The cylindrical coordinate system used to discretize the phantom is shown in (B).

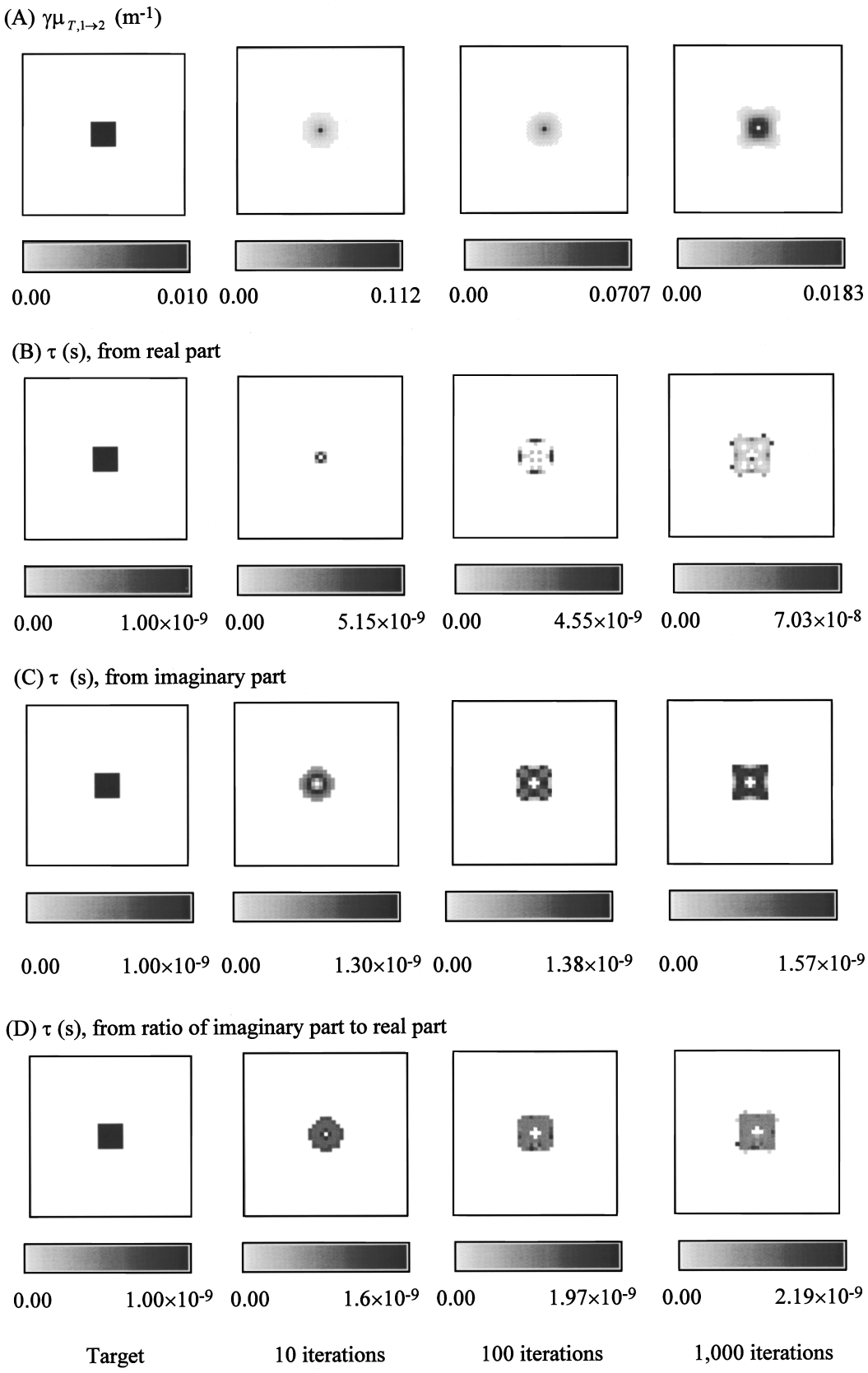

Fig. 4. (A) $\gamma\mu_{T,1\to2}$ images reconstructed from the first set of computed data at the dc frequency. (B)–(D) Reconstructed images of the mean lifetime derived from the parts of the unknowns in Eq. (11) from the first set of computed data as labeled, after 10, 100, and 1000 iterations. The reconstruction algorithm used was CGD, the modulation frequency was 100 MHz, and concentration correction was used.

were invariant in the z direction for z between -3 and 3 mm, and we summed the weights of the voxels along the z axis in this range to obtain integrated values. Only the central planes of the reconstruction results are displayed. Figure 3(B) is an illustration of the cylindrical coordinate systems, where the ρ and the ϕ coordinates are shown and the z coordinate is normal to the plane of the figure. There are 400 voxels in each plane. Reconstructions of $\gamma\Sigma_{T,1\rightarrow 2}N_0$ were performed for both simulation data and experimental data, but mean-lifetime reconstructions were attempted only for the simulation data.

The reconstructed $\gamma\Sigma_{T,1\rightarrow 2}N_0$ were also used to guide the mean-lifetime reconstructions. Inspection of Eqs. (11) and (12) indicates that, in principle, the mean lifetime can be derived directly from the ratio of the imaginary part to the real part of either equation's unknown and does not require any knowledge of $\gamma\Sigma_{T,1\rightarrow 2}N_0$. However, for a numerical reason explained below (see Section 5) we adopted a concentration correction to make additional use of the $\gamma\Sigma_{T,1\rightarrow 2}N_0$ information. The maximum value of each $\gamma\Sigma_{T,1\rightarrow 2}N_0$ map was first obtained, and any value less than 0.01 times this was set to zero. This modified $\gamma\Sigma_{T,1\rightarrow 2}N_0$ map was then used in the calculation of the weight matrix for the corresponding mean-lifetime reconstruction.

4. RESULTS

Figure 4 shows reconstructed images of $\gamma\Sigma_{T,1\rightarrow 2}N_0$ [Fig. 4(A)] and gives results of mean-lifetime reconstructions derived from the reconstructed real part [Fig. 4(B)], imaginary part [Fig. 4(C)], and ratio of imaginary part to real part [Fig. 4(D)] of Eq. (11) from the first set of simulated data (centered inclusion) after 10, 100, and 1000 iterations, by the CGD method with the concentration correction. Figure 5 shows the reconstruction results from the second set of simulation data (off-centered inclusion) after 10, 100, and 1000 iterations by the same method. The reconstruction results obtained without the concentration correction are presented in Fig. 6. Figure 7 shows the reconstruction results obtained from the experimental data by the SART method after 10, 100, 1000, and 10,000 iterations.

5. DISCUSSION AND SUMMARY

Inspection of Fig. 4(A) shows that the size and the location of $\gamma\mu_{T,1\rightarrow 2}$ from the first set of simulation data are successfully reconstructed. There is some error present in that the central part of the inclusion is not reconstructed. Comparison of the images after 10, 100, and 1000 iterations shows that this error grows with increasing computation. This may be a consequence of the structure of the weight function, which steadily decreases with increasing depth such that the voxels with the smallest weights (i.e., those in the center) are overshadowed by surrounding voxels with larger weights. The same phenomenon was observed in the mean-lifetime reconstructions [Figs. 4(B)–4(D)]. The spatial extent of the reconstructed τ is slightly larger than that of the reconstructed $\gamma\mu_{T,1\rightarrow 2}$. We believe that this result is due to the additional numerical processing required for deducing τ from the complex quantity obtained directly from Eq. (11). More specifically, the operation of computing the reciprocals of the real and the imaginary parts may produce large errors in the determination of τ, particularly in voxels for which the true value of the unknown is zero but the numerical result is a small nonzero number.

In general, the reconstruction results for the off-center-inclusion case (Figs. 5 and 6) are less accurate than those for the centered inclusion (Fig. 4). Whereas the lumiphore is uniformly distributed in the inclusion, the reconstructed image values are higher on the side facing the center of the ROI. This may be an effect of the weight-versus-depth relation, just as the central hole in the image of the centered inclusion presumably is. Voxels located on the interior edge of the target have much smaller weights and thus can be assigned erroneous values in the reconstruction without significantly influencing the minimization of mean-squared error. This is one more illustration of the ill-conditioned nature of the weight function in optical tomography.

The error that can result from computing the reciprocals of small values becomes apparent when we compare the mean-lifetime spatial distributions reconstructed with (Fig. 5) and without (Fig. 6) the concentration correction. When this correction was not made the images (Fig. 6) derived from the real part, the imaginary part, and their ratio according to Eq. (11) contain large regions of vastly overestimated τ between the inclusion and the border of the ROI. This finding is consistent with the hypothesis described in the previous paragraph, that the reciprocals of small residual values left over after imperfect cancellations give rise to large errors in the mean-lifetime reconstructions. It is important to note, however, that the concentration correction described here is premised on the assumption that the unknown reconstructed from the dc data is proportional to N_0, which is true only if lumiphore saturation is negligible. If saturation needs to be considered, then the dc reconstruction yields a quantity proportional to N_g, which could be significantly less than N_0. So a low value for N_g in a voxel does not necessarily imply that there is little lumiphore present in the voxel, and a more sophisticated concentration correction than the one presented here must be developed.

It is also observed from Fig. 5 that all errors in the reconstructed images gradually diminish as the number of iterations increases. The images of both $\gamma\mu_{T,1\rightarrow 2}$ and τ are displaced toward the center of the ROI, relative to the true location of the inclusion, after only 10 iterations, but the location is much more accurate after 1000 iterations. From the numerical gray scales we also see that, although the quantitative value of $\gamma\mu_{T,1\rightarrow 2}$ in the inclusion (0.01 m^{-1}) is overestimated, the error decreases as the number of iterations increases. The accuracy of the reconstruction would be expected to improve more if the number of iterations were increased further.

The results from the experimental data (Fig. 7) show that the balloon is located and artifacts are present on the boundary. The inclusion is not clearly identifiable until after 1000 iterations. When other reconstruction algorithms, CGD and POCS, were used (results not shown), a smaller number of iterations was required before the in

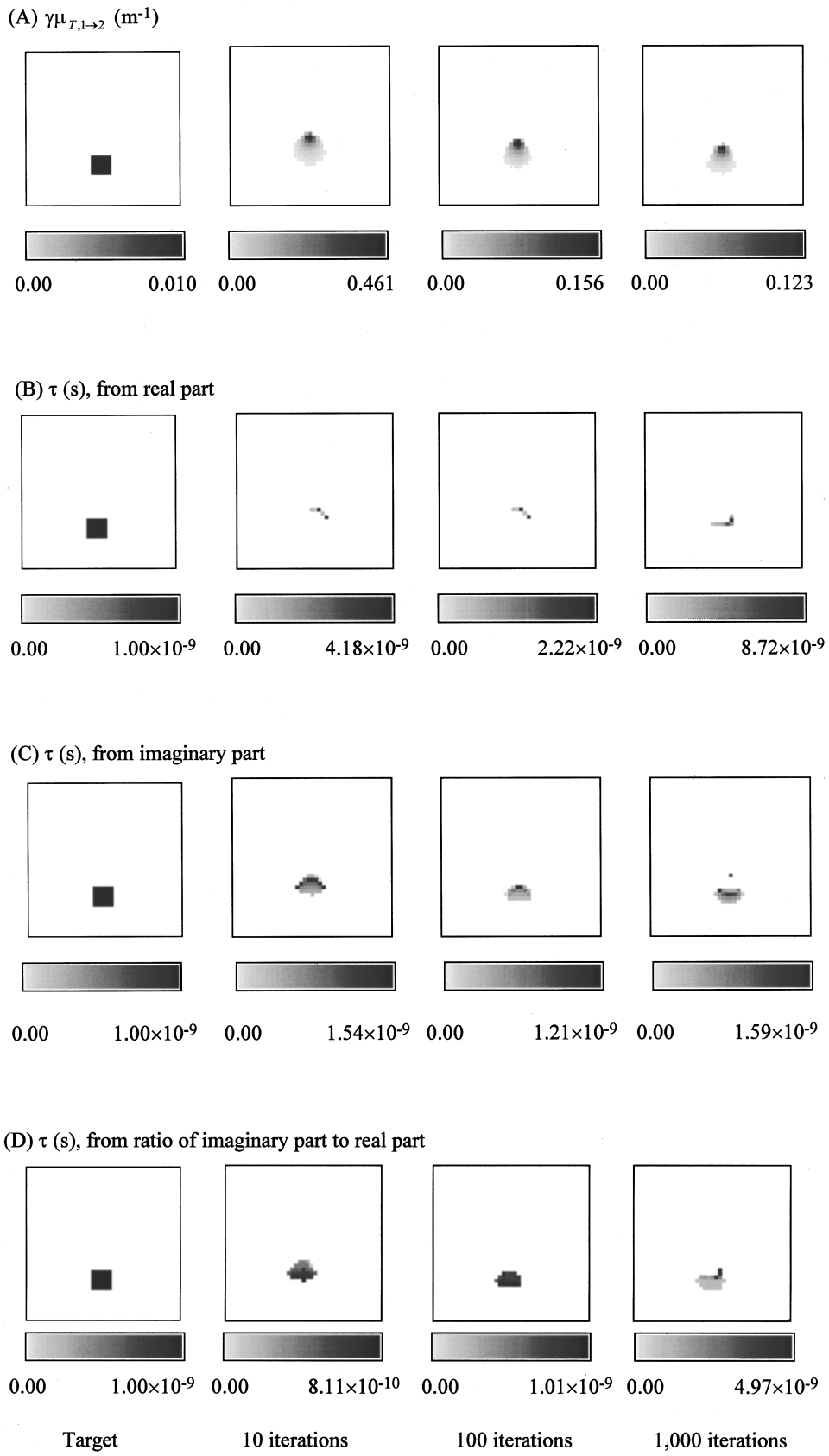

Fig. 5. (A) $\gamma\mu_{T,1\to2}$ images reconstructed from the second set of computed data at the dc frequency. (B)–(D) reconstructed images of the mean lifetime derived from parts of the unknowns in Eq. (11) from the second set of computed data as labeled, after 10, 100, and 1000 iterations. The reconstruction algorithm used was CGD, the modulation frequency was 100 MHz, and concentration correction was used.

clusion was distinguishable, but the SART algorithm pro vides the most accurate intensity mapping. Because different algorithms take widely different pathways in updating the reconstruction and only a finite number of iterations is allowed, these differences among the reconstruction results and convergence rates, especially when range constraints are applied, are not surprising. The intensity of the inclusion reconstructed by the SART algorithm is relatively uniform, with the highest value located in the center of the inclusion. This is unlike the shadowing effect observed in the simulation reconstructions, in which the voxels lying closest to the geometric center of the ROI usually have the largest image values. As the size of the experimental phantom, ~40 transport mfp in diameter, is smaller than that of the simulation phantom, ~80 transport mfp, the shadowing effect plays a less significant role in the experimental reconstruction.

In summary, we have presented a derivation of imaging operators, based on two coupled transport equations, for imaging luminescence in turbid media. Numerical simulations and experiments were performed, and concentration and mean-lifetime images were reconstructed. The proposed concentration correction proved to be crucial for accurate reconstruction of mean lifetime. The reconstruction results from the experimental data are encouraging because they demonstrate that, with added

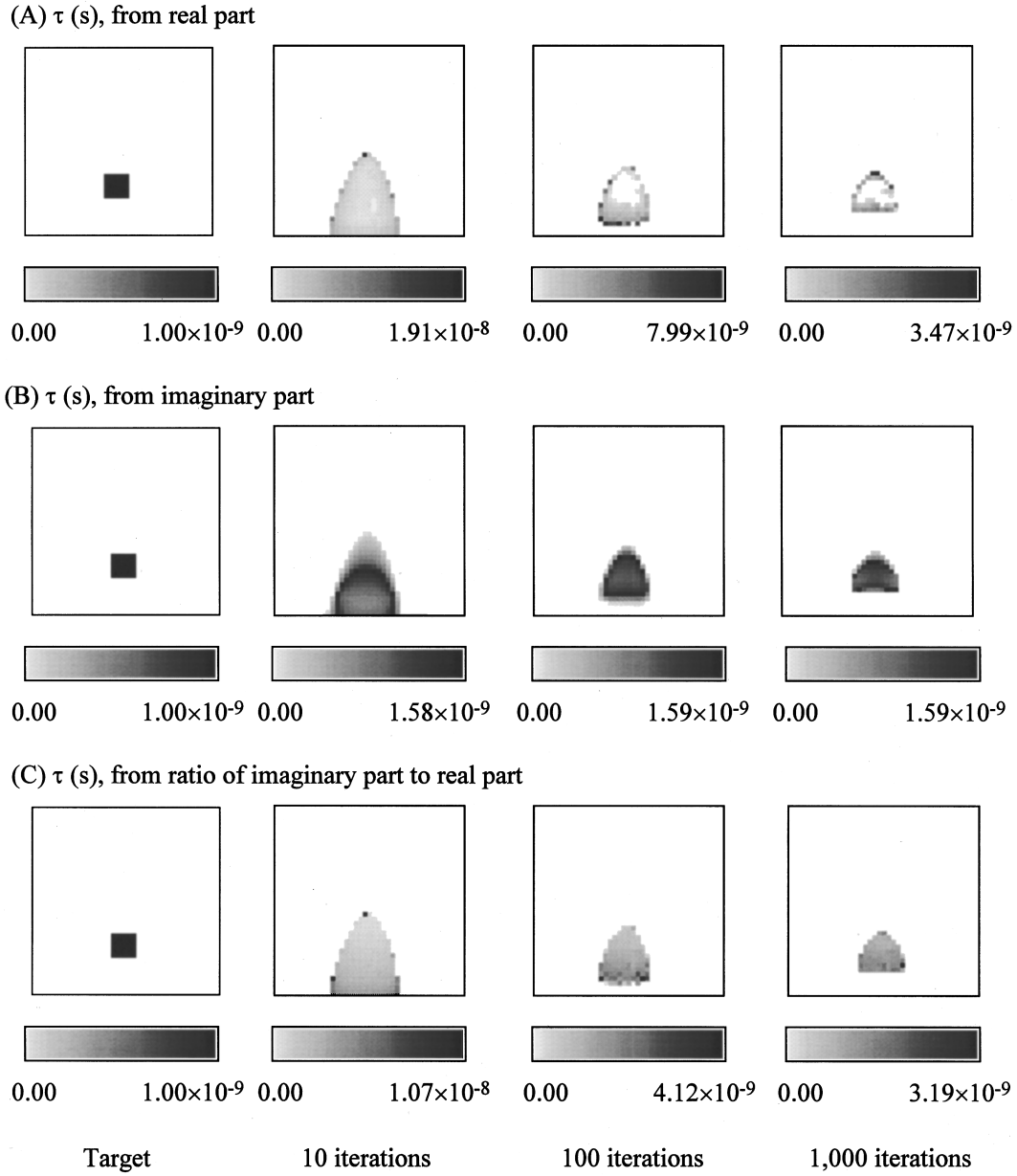

Fig. 6. Reconstructed images of the mean lifetime derived, without the concentration correction, from the parts of unknowns in Eq. (11) as labeled, from the second set of computed data, after 10, 100, and 1000 iterations. The reconstruction algorithm used was CGD, and the modulation frequency was 100 MHz.

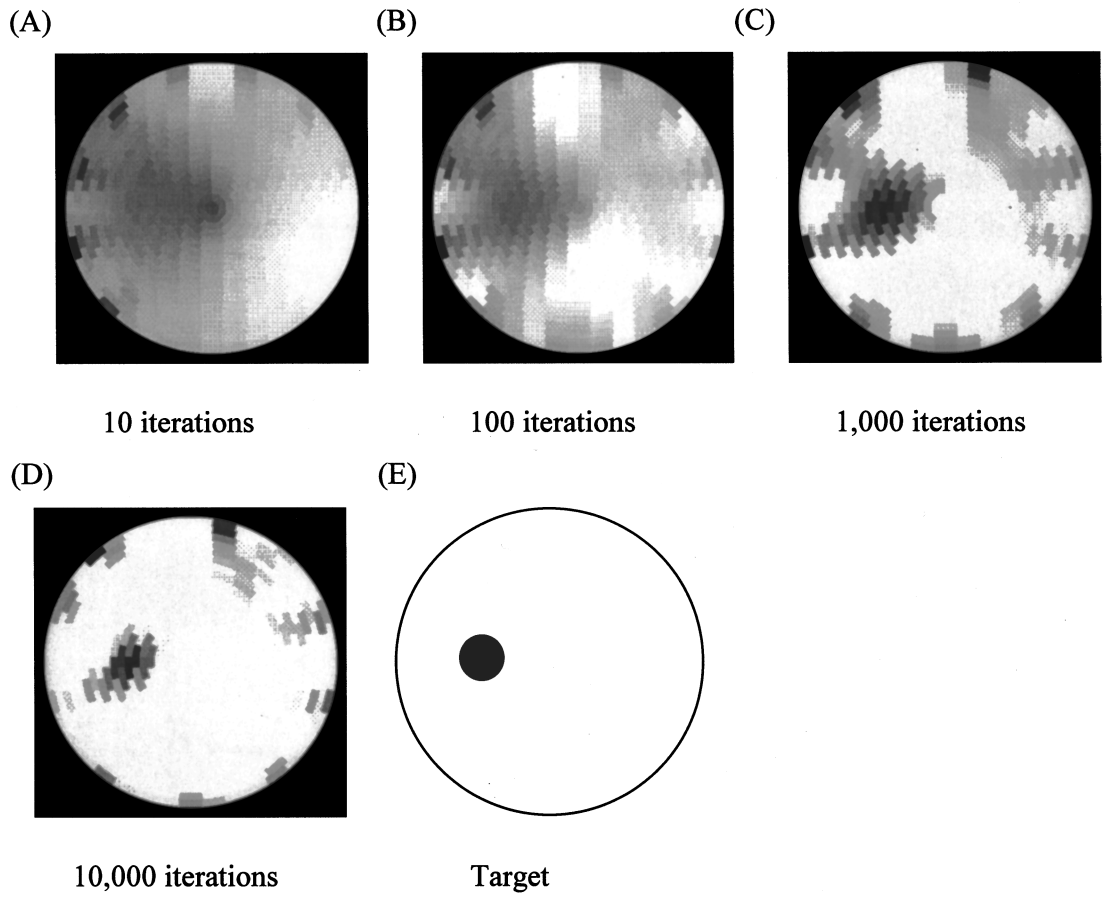

Fig. 7. Reconstruction results obtained from the experimental dc data by the SART after the number of iterations shown. The target is also shown.

background lumiphore, reasonable reconstructions can be achieved from tomographic measurement data.

APPENDIX A: JUSTIFICATION OF EQ. (3)

The luminescence phenomenon entails transitions among (at least) three energy levels: the ground state g and two excited states e_1 and e_2, with e_2 having the highest energy. The three physical processes that are responsible for interlevel transitions are absorption, spontaneous emission, and induced emission. Thus we have

$$\begin{aligned}\frac{dN_g}{dt} &= -\Sigma_{T,1\to 2}\bar{\phi}_1(N_g - N_{e_2}) + \frac{1}{\tau}N_{e_1} \\ &\quad - (N_g - N_{e_1})\int_\omega \Sigma'_{T,2}\bar{\phi}_2 d\omega, \\ \frac{dN_{e_1}}{dt} &= \frac{1}{\tau'}N_{e_2} - \frac{1}{\tau}N_{e_1} + (N_g - N_{e_1})\int_\omega \Sigma'_{T,2}\bar{\phi}_2 d\omega, \\ \frac{dN_{e_2}}{dt} &= \Sigma_{T,1\to 2}\bar{\phi}_1(N_g - N_{e_2}) - \frac{1}{\tau'}N_{e_2}, \end{aligned} \tag{A1}$$

where $\Sigma'_{T,2}$ is the (frequency-dependent) microscopic absorption cross section of the lumiphore for the emission light and τ' is the mean lifetime of a lumiphore molecule in state e_2.

We assume that the final right-hand side terms in the equations for dN_g/dt and dN_{e_1}/dt can be neglected. This assumption is valid if either of two criteria is satisfied, namely, if $\Sigma'_{T,2}$ is essentially zero, i.e., there is insignificant overlap between the absorption and emission spectra of the lumiphore,[14] or if N_0 is small at all points in the medium. The first two terms on the right-hand sides of Eqs. (A1) decrease linearly with decreasing N_0, but, because $\bar{\phi}_2$ is also proportional to N_0, the terms containing $\bar{\phi}_2$ decrease quadratically.

The lumiphore concentrations are constrained by the relation $N_g + N_{e_1} + N_{e_2} = N_0$. Thus only two of Eqs. (A1) should be retained because the third contains no additional information. Retaining the first and the second, and substituting $N_0 - N_g - N_{e_1}$ for N_{e_2}, we obtain the following inhomogeneous system:

$$\frac{d}{dt}\begin{bmatrix} N_g \\ N_{e_1} \end{bmatrix} = \begin{bmatrix} -2\Sigma_{T,1\to 2}\bar{\phi}_1 & (\tau^{-1} - \Sigma_{T,1\to 2}\bar{\phi}_1) \\ -\tau'^{-1} & -(\tau^{-1} + \tau'^{-1}) \end{bmatrix}\begin{bmatrix} N_g \\ N_{e_1} \end{bmatrix} + \begin{bmatrix} \Sigma_{T,1\to 2}\bar{\phi}_1 N_0 \\ \tau'^{-1} N_0 \end{bmatrix}. \tag{A2}$$

Equation (A2) reduces to a single equation, Eq. (3), if we assume that induced emission from e_2 makes a negligible contribution to dN_g/dt, i.e., if $N_{e_2} \ll N_g$. Suppose that the lumiphore were subjected to constant-intensity

illumination. From the third of Eqs. (A1), we find that $\bar{\phi}_1 = (\tau' \Sigma_{T,1\to 2})^{-1}[N_{e_2}/(N_g - N_{e_2})]$ in the resulting steady state. We have assumed a value of $\Sigma_{T,1\to 2} = 5 \times 10^{17}$ cm^2, and we also assume that $\tau' = 1 \times 10^{-12}$ s.[14] Then, for $N_{e_2} = 0.001 N_g$, $0.005 N_g$, $0.01 N_g$, the required $\bar{\phi}_1$ is, respectively, 2.002×10^{25}, 1.005×10^{26}, or 2.020×10^{26} cm^{-2} s^{-1}. At the same three excitation intensities the respective degrees of lumiphore saturation are ~50%, ~83%, and ~91% (for $\tau = 1 \times 10^{-9}$ s). Thus it is easily possible to select $\bar{\phi}_1$ for which saturation of luminescence is significant while emission induced by the excitation light is negligible.

APPENDIX B: DERIVATION OF EQS. (9)

Let us substitute the expression given in Section 2 for time-harmonic illumination, $2\pi \bar{\phi}_1^{\,0}[\delta(\omega) + \eta' \delta(\omega - \omega_0) + \eta'' \delta(\omega + \omega_0)]$, for $\bar{\bar{\phi}}_1$ into Eq. (7a). This gives us

$$2\pi N_0 \delta(\omega) = \tau \Sigma_{T,1\to 2} \bar{\phi}_1^{\,0}[\eta' \tilde{N}_g(\omega - \omega_0) + \eta'' \tilde{N}_g(\omega + \omega_0)] + (1 + \tau \Sigma_{T,1\to 2} \bar{\phi}_1^{\,0} + j\omega\tau) \tilde{N}_g(\omega). \tag{B1}$$

When ω=0, Eq. (B1) becomes

$$2\pi N_0 \delta(0) = (1 + \tau \Sigma_{T,1\to 2} \bar{\phi}_1^{\,0}) \tilde{N}_g(0) + \tau \Sigma_{T,1\to 2} \bar{\phi}_1^{\,0}[\eta' \tilde{N}_g(-\omega_0) + \eta'' \tilde{N}_g(\omega_0)]. \tag{B2}$$

By using the relations $\eta' = \eta''^*$, $\tilde{N}_g(-\omega_0) = [\tilde{N}_g(\omega_0)]^*$, $a^* b^* = (ab)^*$, and $a + a^* = 2\,\Re(a)$, from Eq. (B2) we obtain

$$\Re[\eta'' \tilde{N}_g(\omega_0)] = \frac{2\pi N_0 \delta(0) + (1 + \tau \Sigma_{T,1\to 2} \bar{\phi}_1^{\,0}) \tilde{N}_g(0)}{2\tau \Sigma_{T,1\to 2} \bar{\phi}_1^{\,0}}. \tag{B3}$$

When $\omega = \omega_0$, Eq. (B1) becomes

$$(1 + \tau \Sigma_{T,1\to 2} \bar{\phi}_1^{\,0} + j\omega_0\tau) \tilde{N}_g(\omega_0) + \tau \Sigma_{T,1\to 2} \bar{\phi}_1^{\,0}[\eta' \tilde{N}_g(0) + \eta'' \tilde{N}_g(2\omega_0)] = 0. \tag{B4}$$

If the second-order harmonic can be ignored, i.e., $|\tilde{N}_g(2\omega_0)| \ll |\tilde{N}_g(0)|, |\tilde{N}_g(\omega_0)|$, then

$$\tilde{N}_g(\omega_0) \approx \frac{-\tau \Sigma_{T,1\to 2} \bar{\phi}_1^{\,0} \eta' \tilde{N}_g(0)}{1 + \tau \Sigma_{T,1\to 2} \bar{\phi}_1^{\,0} + j\omega_0\tau}, \tag{B5}$$

which when multiplied by η'' gives

$$\Re[\eta'' \tilde{N}_g(\omega_0)] \approx \frac{-\tau \Sigma_{T,1\to 2} \bar{\phi}_1^{\,0} (\eta/2)^2 (1 + \tau \Sigma_{T,1\to 2} \bar{\phi}_1^{\,0}) \tilde{N}_g(0)}{(1 + \tau \Sigma_{T,1\to 2} \bar{\phi}_1^{\,0})^2 + (\omega_0\tau)^2}. \tag{B6}$$

By equating the right-hand sides of Eq. (B3) and relation (B6) and solving for $\tilde{N}_g(0)$ we get Eq. (9a). When Eq. (9a) is substituted into Eq. (7b) and $\tilde{N}_g(\omega_0)$ is solved for, the result obtained is Eq. (9b).

This recursive procedure can be truncated at a higher-order term, instead of the second-order harmonic as in this derivation, for more-accurate expressions for the saturation correction.

ACKNOWLEDGMENTS

This research is supported in part by National Institutes of Health grant R01-CA59955, by the New York State Science and Technology Foundation, and by U.S. Office of Naval Research grant N000149510063.

REFERENCES

1. G. J. Müller, B. Chance, R. R. Alfano, S. R. Arridge, J. Beuthan, E. Gratton, M. Kaschke, B. R. Masters, S. Svanberg, and P. van der Zee, eds., *Medical Optical Tomography: Functional Imaging and Monitoring*, Vol. IS11 of Institute Series of SPIE Optical Engineering (Society of Photo-Optical Instrumentation Engineers, Bellingham, Wash., 1993).
2. R. R. Alfano, ed., *Advances in Optical Imaging*, Vol. 21 of OSA Proceedings Series (Optical Society of America, Washington, D.C., 1994).
3. B. Chance and R. R. Alfano, eds., *Optical Tomography: Photon Migration and Spectroscopy of Tissue and Model Media: Theory, Human Studies, and Instrumentation*, Proc. SPIE **2389**, 2–874 (1995).
4. J. Chang, H. Graber, R. Aronson, and R. L. Barbour, "Fluorescence imaging using transport-theory-based imaging operators," in *1995 IEEE Engineering in Medicine and Biology 17th Annual Conference* (Institute of Electrical and Electronics Engineers, New York, 1995), abstract 2.3.2.14.
5. J. Chang, R. L. Barbour, H. Graber, and R. Aronson, "Fluorescence optical tomography," in *Experimental and Numerical Methods for Solving Ill-Posed Inverse Problems: Medical and Nonmedical Applications*, R. L. Barbour, M. J. Carvlin, and M. A. Fiddy, eds., Proc. SPIE **2570**, 59–72 (1995).
6. M. A. O'Leary, D. A. Boas, X. D. Li, B. Chance, and A. G. Yodh, "Fluorescence lifetime imaging in turbid media," Opt. Lett. **21**, 158–160 (1996).
7. Y. Paithankar and E. M. Sevick-Muraca, "Fluorescence lifetime imaging with frequency-domain photon migration measurement," in *Biomedical Optical Spectroscopy and Diagnostics*, Vol. 3 of Trends in Optics and Photonics (Optical Society of America, Washington, D.C., 1996), pp. 155–157.
8. P. E. Gill, W. Murray, and M. H. Wright, *Practical Optimization* (Academic, New York, 1981).
9. A. H. Anderson and A. C. Kak, "Simultaneous algebraic reconstruction technique (SART): a superior implementation of the ART algorithm," Ultrason. Imag. **6**, 81–94 (1984).
10. A. V. Kak and M. Slaney, *Principles of Computerized Tomographic Imaging* (Institute of Electrical and Electronics Engineers, New York, 1988), Chap. 7, pp. 285–292.
11. H. H. Rossi, R. G. Alsmiller, Jr., M. J. Berger, A. M. Kellerer, W. C. Roesch, L. V. Spencer, and M. A. Zaider, *Conceptual Basis for Calculations of Absorbed-Dose Distribution*, Rep. 108, National Council for Radiation Protection, Bethsda, Md., 1991).
12. H. C. van de Hulst, *Multiple Light Scattering: Tables, Formulas, and Applications* (Academic, New York, 1980), Vol. 1, Chap. 3, pp. 16–23.
13. J. Chang, R. Aronson, H. L. Graber, and R. L. Barbour, "Imaging diffusive media using time-independent and time-harmonic sources: dependence of image quality on imaging algorithms, target volume, weight matrix, and view angles," Ref. 3, pp. 448–464.
14. J. R. Lakowicz, *Principles of Fluorescence Spectroscopy* (Plenum, New York, 1983), Chap. 1, pp. 1–15.

15. H. J. van Staveren, C. J. M. Moes, J. van Marle, S. A. Prahl, and M. J. C. van Gemert, "Light scattering in Intralipid-10% in the wavelength range of 400–1100 nm," Appl. Opt. **30**, 4507–4514 (1991).
16. J. Chang, H. L. Graber, and R. L. Barbour, "Dependence of optical diffusion tomography image quality on image operator and noise," in *Conference Record of the 1995 IEEE Nuclear Science Symposium and Medical Imaging Conference* (Institute of Electrical and Electronics Engineers, New York, 1996), pp. 1524–1528.
17. J. Chang, H. L. Graber, and R. L. Barbour, "Image reconstruction of dense scattering media from CW sources using constrained CGD and a matrix rescaling technique," Ref. 3, pp. 682–691.